

Crack Growth Simulation in Integrally Stiffened Structures Including Residual Stress Effects from Manufacturing. Part I: Model Overview

S.M. Häusler¹, P.M. Baiz², S.M.O. Tavares³, A. Brot⁴
P. Horst¹, M.H. Aliabadi², P.M.S.T. de Castro³ and Y. Peleg-Wolfin⁴

Abstract: This article represents the first part of a two-part article which presents, compares and discusses the different crack growth simulation models which were introduced for fatigue crack growth assessment during the DaToN project. The project was funded by the EC within the 6th framework program and was specifically devoted to investigate innovative manufacturing techniques for metallic structures with special focus on the effects of residual stresses on the fatigue crack growth and residual strength behaviour. Within this first part the different simulation approaches, including the residual stress modelling approaches will be introduced and stress intensity factor results will be presented and compared. Within this context it could be observed that residual stress effects do have a significant influence on the resulting stress intensity factor solution whose magnitude strongly depends on the input parameters (residual stress field input) but also, to certain extent, on the simulation approaches for stress intensity factor determination as well as residual stress modelling. The residual stress effect also plays an important role for the fatigue crack growth simulations which will be presented in detail in the second part including a comparison with fatigue crack growth results from experiments.

Keywords: stress intensity factor, residual stresses, fatigue crack growth, crack propagation simulation.

1 Introduction

Due to the loading characteristics of a commercial aircraft fuselage, commonly suffering an inside pressurization in combination with maneuver and gust loads during

¹ Technische Universität Braunschweig, Germany. (IFL)

² Imperial College London, UK. (IMPERIAL)

³ Universidade do Porto, Portugal. (IDMEC)

⁴ Israel Aerospace Industries (IAI)

service, the design of specific fuselage parts is governed by different design criteria. For fuselage sections that are predominantly loaded under tension loads the occurrence of cracks and their growth in service represents the major design criteria, which is normally satisfied by ensuring that the growth of occurring cracks is slow enough so that they are found during standard inspection intervals. Innovative manufacturing techniques, especially joining techniques like Laser Beam Welding (LBW) and Friction Stir Welding (FSW), enable new integral fuselage designs with possible savings with respect to manufacturing time and cost and are already applied within fuselage parts primarily being subjected to in-plane pressure loads (e.g. lower fuselage shells of the Airbus A318 and Airbus A380). For tension loaded fuselage parts however, moving from differential to integral designs has a detrimental effect on the fatigue crack growth (FCG) behaviour due to the loss of the previously available second load path given by differentially attached stringers and frames which significantly reduces the number of bearable load cycles and consequently requires special attention and increased reliability of fatigue crack growth simulations.

The most common approach to simulate the fatigue crack behaviour is based on the concept of stress intensity factors (SIF) which characterize the severeness of a cracked configuration and can be determined using different approaches (e.g. VCCT, CTOD, J -integral, empirical solutions).

The above mentioned joining techniques (LBW and FSW) affects the fatigue crack growth behaviour within integrally stiffened structures. Impeded shrinkage of locally heated material at the "weld" line from the joining process, caused by the non-heated surrounding material, introduces residual stresses into the stiffened structure which can considerably affect the fatigue crack growth behaviour of occurring cracks. Reliable fatigue crack growth predictions for such structures should therefore include these effects since they can be both beneficial as well as detrimental. The incorporation of residual stress effects therefore represents one of the main aspects of the present work. However, the investigation of residual stress (RS) effects within this context is limited to those residual stresses that result from the mentioned manufacturing process.

A variety of different techniques for stress intensity factor evaluation will be presented in the following sections together with several different approaches that aim at an incorporation of residual stress effects. These models vary in their degree of detail, complexity and effort (numerical as well as modelling). All approaches will be presented and will be applied to the same problem (two-stiffener aircraft fuselage panel) which enabled a reasonable comparison and discussion with respect to the above mentioned differences in complexity, detail and effort. The methods to be presented are a standard finite element procedure, a p-version FEM, a bound-

ary element procedure and a semi-analytical approach. In addition to the above mentioned joining techniques (LBW and FSW) stiffened panels manufactured by High Speed Cutting (HSC) will be investigated as well, representing a configuration without residual stresses only using the basic simulation models. As a result of being reinforced with stiffeners on only one side, significant bending effects can be observed for the two stiffener panel under investigation which exhibits secondary bending in longitudinal and transversal direction. These bending effects lead to considerable out-of-plane deformations resulting in specific demands for the numerical simulations. Detailed simulations can be ensured by either performing geometrically non-linear simulations which are able to adequately represent the displacement state, or by efficiently restricting the out-of-plane deformation by applying additional constraints in the numerical models which restrict out-of-plane deformation locally (e.g. anti-bending devices) or globally at the complete non-stiffened side of the stiffened panel.

The residual stress model approaches are all based on the basic principle of superposition using different but equivalent approaches for implementation. This comprises applied initial (residual) stresses in combination with standard finite elements, adapted residual stress loading on the crack faces and a weight function method for evaluation of the residual stress intensity factor.

The different modelling techniques, each of them using a different residual stress implementation, in combination with the large experimental data basis that was investigated within the project, lead to a large variety of results associated with different complexity and effort that will be presented and discussed.

This first part of the two-part article will also present the stress intensity factor (SIF) solutions with and without consideration of residual stress effects in order to illustrate the influence of residual stress effects and justify the efforts to include them into simulation tools. The simulation models and the SIF results will be compared and discussed, while the second part will present the fatigue crack growth simulation results including the determination of crack growth parameter sets required for the simulation models and a comparison with experimental fatigue crack growth results that were recorded during the project.

2 Basic simulation approaches and models

2.1 Modified virtual crack closure technique (mVCCT)

The virtual crack closure technique (VCCT) was proposed by Rybicki and Kaninen (1977) in order to calculate the energy release rate (G) based upon the calculation of the strain energy release rate (U). From the energy variation when a virtual extension of crack length is imposed (Δa) the energy release rate can be

approximated by the following equation:

$$G = \frac{\partial U}{\partial a} \approx \frac{U_{a+\Delta a} - U_a}{\Delta a} \quad (1)$$

The application of this concept in finite element models with cracks is done calculating the energy released during an infinitesimal crack tip growth. This energy (ΔE) can be calculated using the nodal loads that are required to maintain the crack increment closed (\mathbf{f}) and the displacement (\mathbf{u}) in the same nodes promoted by removing these loads:

$$\Delta E = \frac{1}{2} (\mathbf{f}\mathbf{u}) \quad (2)$$

The energy release rate is related to the energy release by the area (ΔA) created by the virtual crack extension:

$$G = \frac{\Delta E}{\Delta A} = \frac{\Delta E}{\Delta a t} \quad (3)$$

For plates with constant thickness t , this area is equal to $\Delta a \cdot t$. The energy release rate for each mode of fracture (mode I, II and III) can be determined by the decomposition of the Eq. 2, using the nodal forces and nodal displacements in the direction that characterize each fracture mode. The procedure requires two simulations, one to determine the reaction loads and another to determine the displacements which can be hard working and time consuming in large finite element models. A modified technique of the virtual crack closure technique was presented by Krueger (2002). This modified technique presupposes that the nodal displacements near the crack before and after a sufficiently small crack growth to a crack length of $a + \Delta a$, for nodes equidistant to the crack tip are identical. This assumption allows a calculation of the energy release rate by using only the results from one finite element analysis for each crack length. For 3D quadratic finite elements, the determination of the energy release rate using the modified virtual crack closure technique can be determined using the nodal loads and nodal displacements, however it is required to consider different weights for the nodes being located on the mid-side of the element edge and on the corners of the element. For mode I, considering the annotation presented in Fig. 1, the equation used to determine the energy release rate for the node at the crack surface (node 3) is:

$$G_I = -\frac{1}{4\Delta a\Delta b} \left[\frac{1}{2} F_{z_3} (u_{z_1^*} - u_{z_1}) + \frac{1}{2} F_{z_4} (u_{z_2^*} - u_{z_2}) + F_{z_6} (u_{z_5^*} - u_{z_5}) + \frac{1}{2} F_{z_9} (u_{z_7^*} - u_{z_7}) + \frac{1}{2} F_{z_{10}} (u_{z_8^*} - u_{z_8}) \right] \quad (4)$$

F_z is the nodal force in the z direction, u_z is the displacement in z direction and the Δa and Δb are the element dimensions. For the nodes being positioned in the middle of an element edge, in this case node 6, this gives:

$$G_I = -\frac{1}{2\Delta a\Delta b} \left[F_{z3} (u_{z1^*} - u_{z1}) + \frac{1}{2} F_{z4} (u_{z2^*} - u_{z2}) + \frac{1}{2} F_{z6} (u_{z5^*} - u_{z5}) + \frac{1}{2} F_{z9} (u_{z7^*} - u_{z7}) + \frac{1}{2} F_{z10} (u_{z8^*} - u_{z8}) \right] \quad (5)$$

For the corner nodes inside the crack tip, as e.g. node 9, the energy release rate will be:

$$G_I = -\frac{1}{2\Delta a\Delta b} \left[\frac{1}{2} F_{z6} (u_{z5^*} - u_{z5}) + \frac{1}{2} F_{z9} (u_{z7^*} - u_{z7}) + \frac{1}{2} F_{z10} (u_{z8^*} - u_{z8}) + \frac{1}{2} F_{z12} (u_{z11^*} - u_{z11}) \right] \quad (6)$$

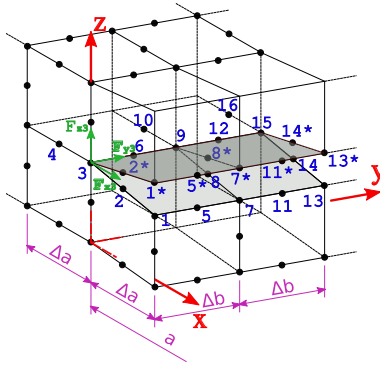


Figure 1: Modified VCCT, annotation and node location for a generic mesh

These three equations are able to determine the evolution of the mode I stress intensity factor along the crack tip in thickness direction. Similar equations for the determination of SIFs in modes II and III can be derived from the above equations by exchanging the nodal loads and nodal displacements according to the associated mode of loading (cp. Krueger (2002)).

2.1.1 Finite element model

A finite element model corresponding to half geometry was made using the symmetry of the DaToN panel and including part of the grip system for better load distribution. This model was processed in ABAQUS Finite Element Analysis software; with 3D quadratic solid elements composed by 20 nodes (C3D20) and 15 nodes (C3D15), ABAQUS (2007). The global model has 47978 elements, 230287 nodes in a total of 690861 variables or equations. Figure 2 shows the mesh of the FE models performed by IDMEC.

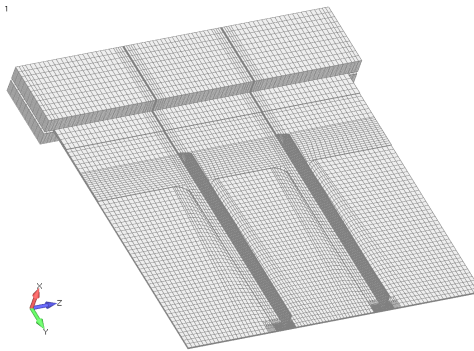


Figure 2: Finite element mesh of DaToN panel - IDMEC models

2.2 *p*-Version FE method

A finite-element model (FEM) was built using StressCheck[®] *p*-version software. StressCheck[®] uses the J-integral method for the computation of mode I and mode II stress intensity factors (SIF), using linear elastic fracture mechanics. The method is super-convergent. This means that the error in the SIF solution converges to zero much faster than the error in the energy norm as the number of degrees-of-freedom is increased. In the vicinity of the crack tip, the solution to the linear problem is singular and the stress values are infinite. Whether or not a crack will propagate, and at what rate, depends on the energy available to drive crack extension. The available energy is characterized by the SIF or the J-integral, which depend on the geometry of the body, the configuration of the crack, the boundary conditions and the loading. In order to reduce the number of elements, a symmetric model was meshed. The calibration of each model was based on strain gauge readings obtained during static load calibration. The SIF was calculated at the crack tip for various crack lengths, using an 8th degree polynomial in the StressCheck[®] FEM. Two phases of the crack growth were analyzed: The first phase consisted of crack growth on the

skin before reaching the integral stiffener. The second phase included two crack paths, one on the skin and another one on the stiffener, as is described below. From the StressCheck[®] stress intensity factor results, a crack growth analysis was performed using NASGRO software. From the StressCheck[®] geometrically nonlinear analysis, the SIF was calculated at the crack tip. A calculation of the SIF was done for each crack step. The crack growth was divided into two phases: Phase 1: Crack growth to the stiffener (one crack tip). Phase 2: Crack growth simultaneously at the skin and at the stiffener (two crack tips). For this phase, a matrix of combinations of skin crack size and stringer crack size was built, to cover all possible combinations of skin crack and stringer crack sizes. NASGRO ver. 5.01, models DT01 (phase 1) and DT03 (phase 2) were used to calculate the predicted life time to failure. It was found that for NASGRO Crack Growth Equation built-in the software, the crack growth data for the AA2024-T351 alloy, has not been fitted optimally for $R = 0.1$. Therefore, a da/dN correction factor of 0.32 was used throughout for the crack growth analysis that uses the p-FEM stress intensity factor results.

2.3 Dual boundary element approach (DBEM)

Boundary integral equations for shear deformable plate analysis can be obtained by coupling Reissner's plate and two-dimensional plane stress theories as follows Aliabadi (2002):

$$c_{ij}(\mathbf{x}')w_j(\mathbf{x}') + \oint_{\Gamma} P_{ij}^*(\mathbf{x}', \mathbf{x})w_j(\mathbf{x})d\Gamma(\mathbf{x}) = \int_{\Gamma} W_{ij}^*(\mathbf{x}', \mathbf{x})p_j(\mathbf{x})d\Gamma(\mathbf{x}) \quad (7)$$

$$+ \int_{\Omega} W_{i3}^*(\mathbf{x}', \mathbf{X})q_3(\mathbf{X})d\Omega(\mathbf{X})$$

and

$$c_{\theta\alpha}(\mathbf{x}')u_{\alpha}(\mathbf{x}') + \oint_{\Gamma} T_{\theta\alpha}^{*(i)}(\mathbf{x}', \mathbf{x})u_{\alpha}(\mathbf{x})d\Gamma(\mathbf{x}) = \int_{\Gamma} U_{\theta\alpha}^*(\mathbf{x}', \mathbf{x})t_{\alpha}(\mathbf{x})d\Gamma(\mathbf{x}) \quad (8)$$

$$+ \int_{\Omega} U_{\theta\alpha}^*(\mathbf{x}', \mathbf{X})q_{\alpha}(\mathbf{X})d\Omega(\mathbf{X})$$

where \oint denotes a Cauchy principal value integral and $\mathbf{x}', \mathbf{x} \in \Gamma$ are source and field points respectively. $c_{ij}(\mathbf{x}')$ represent the jump terms, whose value is equal to $\frac{1}{2}\delta_{ij}$ when \mathbf{x}' is located on a smooth boundary. w_{α} denotes rotations of the middle surface, w_3 out-of-plane displacement, and u_{α} in-plane displacements. Their corresponding tractions are denoted as p_i and t_{α} , and q_i are the body forces. Equations (7)-(8) represent a set of five boundary integral equations. Equations in (7) are for rotations and out-of-plane displacement while equations (8) are for in-plane displacements.

The application of the boundary element method to fracture mechanics presents a problem due to the coincidence of the crack surfaces; making point collocation generates identical equations (ill-conditioned problem). The dual boundary element method (DBEM) is the most efficient way of dealing with this difficulty. DBEM is based on the use of two independent equations, the displacement and traction boundary integral equations, at each pair of coincident source points on the surfaces that define a crack. The traction integral equations for shear deformable plate bending are given as follows Aliabadi (2002):

$$\begin{aligned} & \frac{1}{2}p_i(\mathbf{x}') + n_\beta(\mathbf{x}') \oint_{\Gamma} P_{i\beta j}^*(\mathbf{x}', \mathbf{x}) w_j(\mathbf{x}) d\Gamma(\mathbf{x}) \\ &= n_\beta(\mathbf{x}') \oint_{\Gamma} W_{i\beta j}^*(\mathbf{x}', \mathbf{x}) p_j(\mathbf{x}) d\Gamma(\mathbf{x}) + n_\beta(\mathbf{x}') \int_{\Omega} W_{i\beta 3}^*(\mathbf{x}', \mathbf{X}) q_3(\mathbf{X}) d\Omega(\mathbf{X}) \end{aligned} \quad (9)$$

and for plane stress elasticity

$$\begin{aligned} & \frac{1}{2}t_\alpha(\mathbf{x}') + n_\beta(\mathbf{x}') \oint_{\Gamma} T_{\alpha\beta\gamma}^*(\mathbf{x}', \mathbf{x}) u_\gamma(\mathbf{x}) d\Gamma(\mathbf{x}) \\ &= n_\beta(\mathbf{x}') \oint_{\Gamma} U_{\alpha\beta\gamma}^*(\mathbf{x}', \mathbf{x}) t_\gamma(\mathbf{x}) d\Gamma(\mathbf{x}) + n_\beta(\mathbf{x}') \int_{\Omega} U_{\alpha\beta\gamma}^*(\mathbf{x}', \mathbf{X}) q_\gamma(\mathbf{X}) d\Omega(\mathbf{X}) \end{aligned} \quad (10)$$

Equations (9)-(10) represent five integral equations in terms of boundary tractions, and can be used together with the five displacement integral equations (7)-(8) to form the dual boundary integral formulation. The kernels $W_{i\beta k}^*$, $P_{i\beta k}^*$, $U_{\alpha\beta\gamma}^*$ and $T_{\alpha\beta\gamma}^*$ are linear combination of the first derivatives of the fundamental solutions: W_{ij}^* , P_{ij}^* , $U_{\alpha\beta}^*$ and $T_{\alpha\beta}^*$, respectively. The expression for all these kernels are given in Aliabadi (2002).

As presented by Wen, Aliabadi, and Young (2004) a multi-region DBEM formulation for shear deformable plate bending can be efficiently applied to crack growth analysis in airframe structures. In Wen, Aliabadi, and Young (2004) the behaviour of crack growth on single skin sections was investigated. This formulation was adapted in this work to model cases when skin and stiffeners are simultaneously undergoing a fatigue crack growth process within a residual stress field.

2.3.1 Stress intensity factors in shear deformable plates

In shear deformable plate theory, five stress intensity factors can be defined. The stress intensity factors for a flat plate loaded in combined bending and tension can be represented by superposition of SIFs: two SIFs due to membrane loads, K_{1m} and K_{2m} ; and three SIFs due to bending moments and shear loads, K_{1b} , K_{2b} , and K_{3b} . In the present work, these SIFs are obtained using the *Crack Tip Opening Displacement*(CTOD) and the path independent *J- integral*.

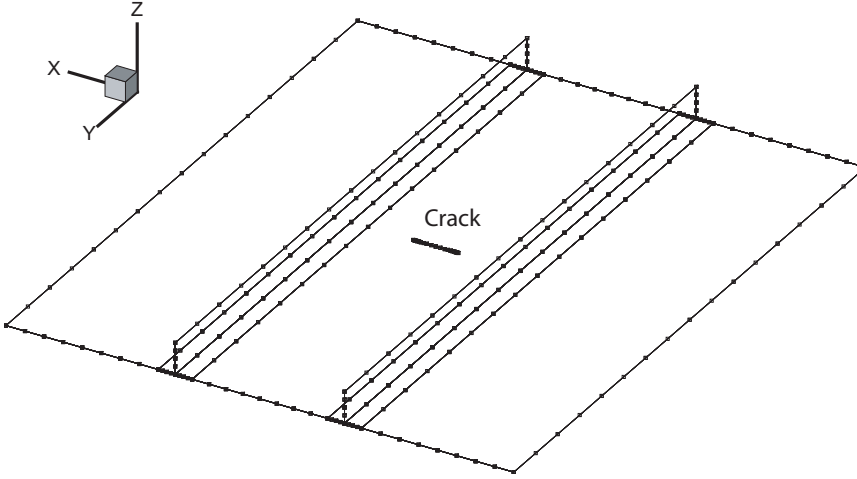


Figure 3: Boundary element mesh of stiffened panel

After SIFs in shear deformable plates are obtained, these can be related to the classical SIF (K_I , K_{II} , and K_{III}) as follows:

$$K_I = \frac{1}{h} K_{1m} + \frac{12x_3}{h^3} K_{1b}; \quad (11)$$

$$K_{II} = \frac{1}{h} K_{2m} + \frac{12x_3}{h^3} K_{2b} \quad (12)$$

$$K_{III} = \frac{3}{2h} \left[1 - \left(\frac{2x_3}{h} \right)^2 \right] K_{3b} \quad (13)$$

2.3.2 DBEM model

The discretized DBEM model of the stiffened panel is shown in Figure 3. For the initial crack size, the model contains 9 plates with 288 boundary nodes. Plate simply supported boundary conditions ($w_3 = 0$) and the maximum stress ($\sigma_{yy} = \sigma^{max}$) are applied on the skin and stiffeners of the panel at $y = 0$ and $y = 540mm$. Additionally, symmetrical constraints are also applied at other points in the panel (avoiding rigid body movement).

2.4 Pseudo-numerical approach (PseudoNum)

The last simulation approach to be presented here uses an analytical approach and consequently differs quite significantly from the methods presented so far. It uses

certain simplifying assumptions (plane state approach, pure Mode I opening mode, limited capabilities to account for bending effects) which lead to a method that is capable to provide fast estimations on the complete fatigue crack growth life of an integrally stiffened structure. The method is based on an approach for riveted structures which was introduced by Swift (1979) and Nishimura (1991) and evaluates the stress intensity factor in a stiffened structure by requiring compatibility of displacements between skin sheet, fasteners and stiffeners (cp. Fig. 4). By solv-

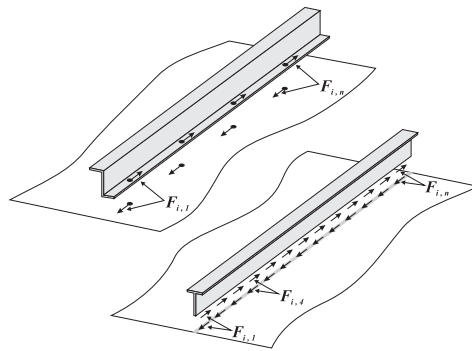


Figure 4: Load transfer mechanisms: built-up (riveted) design (top), integrally stiffened design (bottom)

ing the equation system that results from this compatibility requirement the load transfer forces $F_{i,j}$ acting along the skin-stiffener-interface can be determined and can then be used to determine the stress intensity factors in the skin sheet K_{sk} and stiffener K_{st} via superposition. In order to handle stiffened structures with integral characteristics several adaptations on the original approaches are required. These adaptations primarily affect the case of cracks branching into the stiffeners and the load transfer mechanism between skin and stiffeners. Instead of being transferred at discrete positions, the load is transferred continuously (cp. Fig. 4) within an integral design, which is incorporated by directly adjoining the load transfer positions and adapting the corresponding load transfer areas to the different boundaries defined by the stiffener thickness. Hence, the compatibility equation between skin sheet and stiffening elements reduces to the following expression for the integral case

$$V_{skin} = V_{stiff} \tag{14}$$

where the displacement contributions for skin and stiffener can be further subdivided into contributions due to globally applied stress σ_0 and, locally acting, load

transfer forces $F_{i,j}$.

$$V_{\text{skin}} = V_1(\sigma_0) + V_2(F_{i,j}) + V_3(F_{i,j}) \quad (15)$$

$$V_{\text{stiff}} = V_{G_i}(\sigma_0) + V_{D_i}(F_{i,j}) \quad (16)$$

The single contributions are determined using analytical formulations like for example Westergaard's complex stress function and have to be evaluated at each load transfer position (x_i, y_i) along the skin-stiffener interfaces which leads to a linear equation system of the following type that has to be solved to determine the $F_{i,j}$.

$$\mathbf{C}_{\text{comp}} \mathbf{f}_{\text{comp}} = \mathbf{g}_{\text{comp}} \quad (17)$$

The vector \mathbf{g}_{comp} stores all displacement contributions associated to remote stress σ_0 and the vector \mathbf{f}_{comp} contains the unknown load transfer forces $F_{i,j}$. The compatibility matrix \mathbf{C}_{comp} holds all displacement contributions associated to these $F_{i,j}$ and is fully loaded and in general non-symmetric.

2.4.1 Skin and stiffener stress intensity factors

Having determined the local load transfer forces $F_{i,j}$ by solving the compatibility equation system, the overall stress intensity factors (SIF) for the skin sheet and each stiffener can be obtained by superposition of the stress intensity factors that result from remote stress and load transfer forces. For the stress intensity factor in the skin sheet K_{sk} the SIF from remote stress and the load transfer forces from all stiffeners yield the following expression where n_{st} represents the number of stiffening elements and N_{st} represents the number of load transfer forces per stiffener.

$$K_{sk} = \sigma_0 \sqrt{\pi a_{sk}} - \sum_{i=1}^{n_{st}} \sum_{j=1}^{N_{st}} \frac{F_{i,j}}{t_{sk} \sqrt{\pi a_{sk}}} \left[\frac{I_1 + y_j (1 + \nu_{sk}) I_2}{2 \sqrt{r_1 r_2}} \right] \quad (18)$$

with

$$\begin{aligned} I_1 &= \sqrt{\frac{r_2}{r_1}} \sin \left(\frac{\theta_1 - \theta_2}{2} \right) \\ I_2 &= \cos \left(\frac{\theta_1 + \theta_2}{2} \right) - \frac{r_2}{r_1} \cos \left(\frac{3\theta_1 - \theta_2}{2} \right) + \frac{a}{r_1} \cos \left(\frac{3\theta_1 + \theta_2}{2} \right) \\ r_1 &= \sqrt{(x_i - a_{sk})^2 + y_i^2} & r_2 &= \sqrt{(x_i + a_{sk})^2 + y_i^2} \\ \theta_1 &= \arctan \left(\frac{y_i}{x_i - a_{sk}} \right) & \theta_2 &= \arctan \left(\frac{y_i}{x_i + a_{sk}} \right) \end{aligned}$$

The stress intensity factor $K_{sk,i}$ for each stiffener i is determined in a similar fashion as a result of the remote stress the load transfer forces of the stiffener under investigation by

$$K_{sk,i} = K_{G,i} + \sum_{j=1}^{N_{st}} K_{D,ij} \tag{19}$$

where $K_{G,i}$ and $K_{D,ij}$ in Eq. 19 are the stress intensity factors due to remote stress and load transfer forces in the current stiffener and are expressed using empirical solutions according to the investigated case from Tada, Paris, and Irving (2000). Here $K_{G,i}$ and $K_{D,ij}$ are determined using expressions for edge cracked scenarios illustrated in Fig. 5. This is assumed to result in conservative SIF results for the stiffener since the cracked stiffener in the two stiffener panel is additionally constrained along the cracked edge by the skin sheet which decreases the loading condition on the stiffener crack.

$$K_{G,i} = \sigma_0 \sqrt{\pi a_{st}} \sqrt{\frac{2h}{\pi a_{st}} \tan \frac{\pi a_{st}}{2h}} \left[\frac{0.752 + 2.02 \left(\frac{a_{st}}{h}\right) + 0.37 \left(1 - \sin \frac{\pi a_{st}}{2h}\right)^3}{\cos \frac{\pi a_{st}}{2h}} \right] \tag{20}$$

$$K_{D,ij} = \frac{F_{i,j}}{t_{st} \sqrt{\pi a_{st}}} \frac{1 + 2Y^2}{(1 + Y^2)^{\frac{3}{2}}} \left\{ 1.3 - 0.3X^{\frac{5}{4}} \left[0.665 - 0.267X^{\frac{5}{4}} (X - 0.73) \right] \right\} \tag{21}$$

with

$$Y = \frac{y_j}{a_{st}} \quad \text{and} \quad X = \frac{Y}{\sqrt{1 + Y^2}}$$

2.4.2 Model boundary conditions

A number of 30 load transfer positions was assumed for each stiffener within the compatibility approach which proved to be sufficient for an adequate representation of the incompatibility between skin sheet and stiffener in the range of the crack. Since the load transfer positions are distributed symmetrically with respect to the crack line this leads to 15 load transfer positions per stiffener to be considered in the compatibility equation leading to a compatibility matrix of size $N \times N$ with $N = n_{st} \cdot N_{st} = 2 \cdot 15 = 30$ degrees of freedom. The plane approach does not

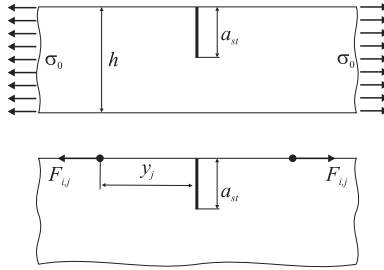


Figure 5: Edge crack scenarios for determination of $K_{G,i}$ (top) and $K_{D,i,j}$ (bottom)

account for out-of-plane displacements in general but longitudinal bending effects are considered within the model by including stiffener displacement contributions resulting from eccentric loading of the stiffeners by the local load transfer forces. No transversal bending effects are considered within the approach which represents a limitation for considerably long cracks which extend beyond the stiffener position where significant bending effects in transversal direction could be observed during experiments and finite element simulations. The applied load is assumed to act uniformly at the free ends of the model in longitudinal direction.

3 Residual stress effects

As has already been mentioned in the introduction and the accompanying articles the DaToN project paid special attention to the investigation of residual stress effects on fatigue crack growth and their incorporation into simulation methods. Residual stresses may be generated or modified at every stage of a component life, from original material production to final disposal. Welding is one of the most significant causes of residual stresses and typically produces large tensile stresses (due to the shrinkage of the weld on cooling) whose maximum value could reach the yield strength of the material. Welding residual stresses not only cause distortion but also significantly affect the performance of welded structures specially for the failures occurring under low applied stresses such as brittle fracture, fatigue, and stress corrosion cracking. Within the DaToN project the focus was set on residual stresses resulting from the manufacturing processes used to attach the stiffeners. The residual stresses introduced by the applied joining techniques (laser beam welding (LBW) and friction stir welding (FSW)) are primarily caused by impeded shrinkage of locally heated material in the weld zones by the surrounding material. According to Wohlfahrt (1987), the residual stresses in Fig. 6 can be observed in longitudinal σ_l and transversal σ_t direction in a perpendicular cut to the weld

line ($x,y=0$) for a simple butt welded panel. Because the project was exclusively devoted to the investigation of cracks propagating perpendicularly to the stiffeners (weldings) under uniaxial loading in the longitudinal direction, corresponding to mode I loading, all following investigations were limited to the effects of the longitudinal residual stresses σ_l . Before a detailed fatigue crack growth analysis of

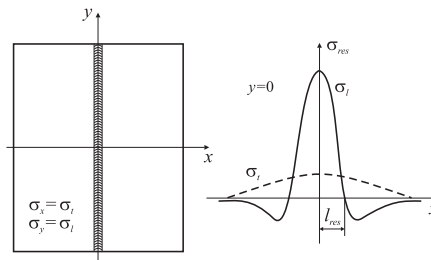


Figure 6: General distribution of longitudinal and transversal residual stresses within a butt welded specimen

the panels considered in this work could be carried out, knowledge of the residual stresses was necessary. Several residual stress fields were considered: experimental, numerical and analytical. Experimental residual stresses were measured at the University of Pisa (Lanciotti, Lazzeri, and Polese, 2008) on different samples by applying strain gauges and subsequently sectioning of the specimen (see Fig. 7 for strain gauge locations). By using a large amount of strain gauge measurements on front side, back side and at the stiffeners very detailed information on the residual stress field distributions could be recorded. In Fig. 8 the longitudinal residual stress distribution is exemplary shown for a laser beam welded configuration of an AA2024 panel for the front and back side strain gauges and the average between those two values. A summary on the experimentally determined residual

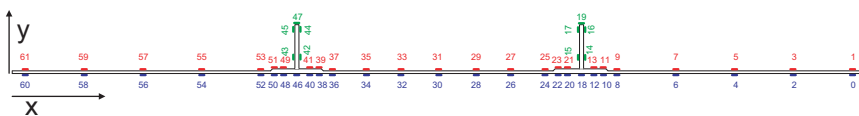


Figure 7: Strain gauge positions for the DaToN two-stiffener panels (Lanciotti, Lazzeri, and Polese, 2008)

stresses are given for AA2024 panels in Fig. 9 and for AA6056 panels in Fig. 10 and a comparison with the empirical RS distribution in Fig. 6 shows very similar

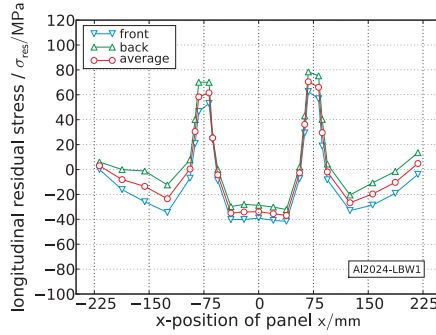


Figure 8: Experimentally determined residual stress field for AA2024-LBW

characteristics around the weld lines at $x = \pm 75\text{mm}$. For reasons of clarity only the mean stress distributions from panel front and back side are shown, emphasizing that the detailed data set (cp. Fig. 8) is available for every configuration (see Lanciotti, Lazzeri, and Polese (2008)). The similar characteristics of empirical,

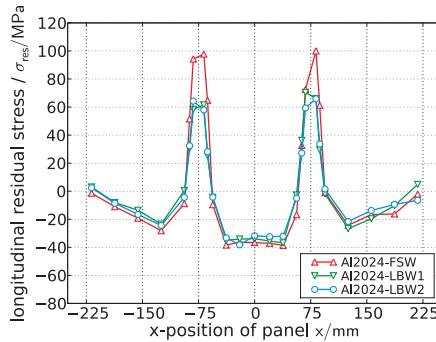


Figure 9: Experimentally determined mean residual stress fields for the DaToN panels made from AA2024

numerically and experimentally determined residual stress field distributions can be represented in a simple analytical form by considering the following empirical residual stress functions proposed by Terada (1976) and Tada and Paris (1983) for standard residual stress distributions in single butt welded specimens.

$$\sigma_{res} = \sigma_{res,0} \cdot f_i(\xi) \quad (22)$$

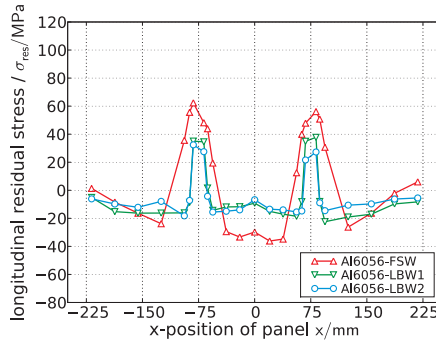


Figure 10: Experimentally determined mean residual stress fields for the DaToN panels made from AA6056

with

$$f_1 = (1 - \xi^2) e^{-0.5\xi^2} \quad \text{Terada (1976)} \quad (23)$$

$$f_2 = \frac{(1 - \xi^2)}{(1 + \xi^4)} \quad \text{Tada (1983)} \quad (24)$$

σ_{res} is the resulting longitudinal residual stress, $\sigma_{res,0}$ represents the maximum tensile residual stress acting directly at the weld line and $\xi = \frac{x}{l_{res}}$ is a normalized coordinate defined as the x -distance from the weld line divided by a characteristic length l_{res} which is defined by the position where the residual stress field enters the compressive region. Both expressions (23) and (24) fulfil the requirements on residual stresses and are self-balanced, symmetric to the weld line with maximum values directly at the weld line and diminishing values far away from the weld line. Due to their simplicity and their good agreement with experimental results the presented empirical expressions form the basis of the approaches in sections 3.1.3 and 3.1.2 which will be presented later on. A numerical residual stress field obtained from a thermo-mechanical simulation performed by the University of Patras (Diamantakos and Tsirkas, 2008) and analytical residual stress fields are given in Fig. 14, Fig. 12 and Fig. 13 in the following sections which were partly presented before by Häusler and Horst (2008).

3.1 Incorporation into simulation models

As already mentioned significant residual stresses could be observed in the integrally stiffened panels manufactured by LBW and FSW which have an impact on

the fatigue crack growth behaviour that could also be observed during the experimental crack growth tests (Lazzeri, Lanciotti, and Polese, 2009) performed in the DaToN project. This section presents the different approaches utilized in order to include the effects of longitudinal residual stresses on fatigue crack growth within the simulation methods presented in section 2. Within this context different implementations will be presented which all share the common idea of superposition. For linear elastic material behaviour, individual components of stress, strain and displacement are additive. In the same way that two normal stresses in the x direction imposed by different external loads can be added to obtain the total σ_{xx} , stress intensity factors are additive as long as the mode of loading is consistent:

$$K_I^{Total} = K_I^{(A)} + K_I^{(B)} + K_I^{(C)} + \dots \quad (25)$$

This property of linear elastic fracture mechanics allows stress intensity factors for complex configurations to be built from simple cases for which the solutions are well established. This principle is used for considering also the effect of residual stresses during the fatigue crack growth simulations within this study leading to a superposition of the stress intensity factors from applied loading K_0 and residual stresses K_{res} , where the index I for mode I is omitted for reasons of readability, so that Eq. 25 becomes

$$K_{total} = K_0 + K_{res} \quad (26)$$

The different methods to determine/incorporate K_{res} represent the main difference between the approaches and will be presented in the following.

3.1.1 3D FE simulations (mVCCT approach)

The residual stress was applied as initial condition in the three dimensional finite element models, using the experimental data obtained by Lazzeri, Lanciotti, and Polese (2009). Since these models are 3D models of the stiffened panel and the measurements were done at the top and bottom surfaces, interpolation techniques were used to apply the residual stress field as initial condition in the FE models. The residual stress can be applied to the 3D solid element types C3D15 and C3D20 from the ABAQUS element library at the centroid position (ABAQUS, 2007). In order to interpolate the residual stress field to the finite element centroids a 3D biharmonic spline interpolation was implemented in MATLAB. The contour map of the initial stress condition (uncracked panel) is presented in Fig. 11. After this initial condition, the remote load and the boundary conditions that define the crack size are applied and the redistribution of the stress field is calculated taking into account the equilibrium of this variable.

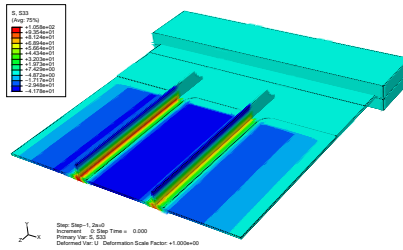


Figure 11: Initial stress condition (residual stress state) for the laser beam welded (LBW) configuration of AA2024-T3

3.1.2 Weight function method (*PseudoNum approach*)

The approach that is used in combination with the analytical approach in 2.4 is similar to the preceding one but directly evaluates the stress intensity factors from residual stresses using an analytical approach introduced by Terada and Nakajima (1985). This method is based on a weight function approach that applies the residual stress field on the crack faces and determines the residual stress intensity factor by integration of the corresponding residual stress field along the crack.

$$K_{res,\pm a} = \frac{1}{\sqrt{\pi a}} \int_{-a}^a F_i(\xi) \frac{\sqrt{a \pm \xi}}{\sqrt{a \mp \xi}} d\xi \quad (27)$$

where the integrand $F_i(\xi)$ is chosen from one of the residual stress field expressions from above. In order to account for the fact that the crack centre does not coincide with the weld line in the present case, ξ has to be replaced with $\xi + L$ in (23) and (24) where L represents the *eccentricity* of the crack, i.e. the distance between crack centre and weld line/stiffener. Taking a closer look on the experimental residual stress field distribution in Fig. 9 and Fig. 10 a fully compressive residual stress field can be observed between the stiffeners which is assumed to result from the interaction of the residual stress fields of the single weldings. Like already mentioned, this compressive stress zone is of significant importance for the fatigue crack growth behaviour but cannot be represented by the original expressions (23) and (24). Therefore the above expressions are modified by introducing two additional parameters in order to include the interaction effects of the residual stress fields from multiple weldings. The first parameter y_{mod} (cp. Eq. (28)) can be considered as a shifting parameter in order to reflect the compressive residual stress field between the stiffeners while the second parameter $\sigma_{mod,0}$ (cp. Eq. (29)) represents a modified maximum residual stress to be substituted for $\sigma_{res,0}$ in the original formulations ((23), (24)) and is needed to compensate the compressive

shifting introduced by y_{mod} .

$$\sigma_{mod,0} = \sigma_{res,0} - \frac{\sigma_{res}^{compr}}{n_{st}} \quad (28)$$

$$y_{mod} = - \left[\frac{(\sigma_{res}^{compr})^2}{n_{st} \sigma_{mod,0}} \right] \quad (29)$$

with σ_{res}^{compr} being the maximum compressive residual stress observed in the experimental solution and n_{st} representing the number of welded stiffeners. The required parameters σ_{res}^{compr} , $\sigma_{res,0}$ and l_{res} are determined from the experimental residual stress distributions given in Lanciotti, Lazzeri, and Polese (2008). Fig. 12 and

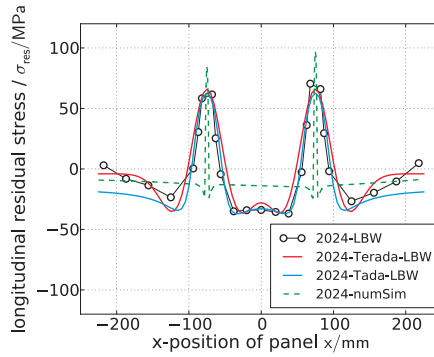


Figure 12: Experimental and empirical residual stress fields for AA2024-LBW used for the weight function method (PseudoNum)

Fig. 13 show the good accordance of the modified residual stress field distributions with experimental results exemplary for a LBW and a FSW configuration. Although theoretically this empirical residual stress representation is not balanced in the structure, it gives a simple and attractive way to represent the behaviour observed on the experimental residual stress fields. Since the modified approach derived on basis of Tada and Paris (1983) provided a better fit for most cases only this approach will be considered in the following. Tab. 1 summarizes the residual stress parameters determined from the experimental results (average RS). These parameters are used in Eqs. (23) and (24) in order to determine the simulation model parameters required for the fatigue crack growth investigations. Resulting fatigue crack growth results are presented in detail in the accompanying article Tavares et al. (2009).

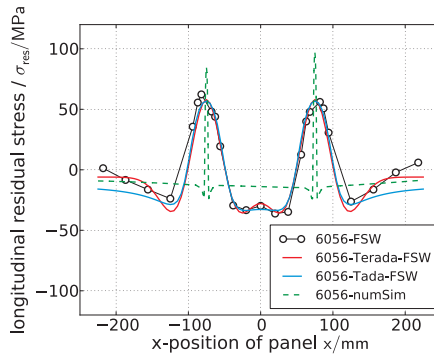


Figure 13: Experimental and empirical residual stress fields for AA6056-FSW used for the weight function method (PseudoNum)

Table 1: Residual stress model parameters used for the weight function approach (PseudoNum)

	AA2024		AA6056	
	FSW	LBW	FSW	LBW
$\sigma_{res,0} / \text{MPa}$	100	66	59	39
l_{res} / mm	25	26	32	15
$\sigma_{res}^{compr} / \text{MPa}$	-40	-37	-36	-19

3.1.3 Crack face loading (DBEM approach)

As already said the advantage of the above presented analytical (standard) residual stress fields (cp. (23) and (24)) is that they are easier to handle than experimental or numerical ones while providing a good agreement with experimental data which is the reason they form the basis of the remaining two methods. The residual stress distributions from Fig. 14 are used to determine direct boundary tractions which are then applied on the crack faces of the DBEM models to achieve equivalent loading conditions resulting from the residual stress field.

$$t_{\alpha}^{res} = N_{\alpha\beta}^{res} n_{\beta} = \sigma_{\alpha\beta}^{res} n_{\beta} h \quad (30)$$

Two DBEM models are run, one model in which only the maximum external loading at the ends is applied (110MPa) and a second case in which the maximum external loading and crack faces boundary tractions (residual stress field) are

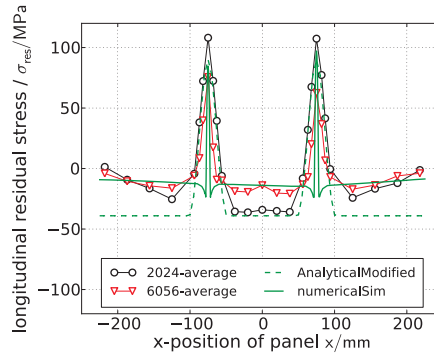


Figure 14: Comparison of experimental, numerical and empirical residual stress fields used for the adapted crack face loading approach (DBEM)

simultaneously applied. Stress intensity factors due only to the residual stress field can be obtained by considering the difference between both results (LEFM).

4 Numerical simulation

This section will present the first part of results that were attained using the above presented simulation approaches. However, the focus here will solely be on stress intensity factor solutions and the effect of residual stresses on these solutions, while the accompanying second part paper (Tavares et al. (2009)) will present results for the fatigue crack growth simulations in large detail including a comparison with experimental results acquired within the project which are presented in detail in Lazzeri, Lanciotti, and Polese (2009).

4.1 Model geometry and specifications

The general dimensions that are common for all configurations of the integral two-stiffener DaToN panel are given in Fig. 15. Two different loading conditions were considered during the study, one scenario at a maximum stress of $\sigma_{\max} = 80\text{MPa}$ and a stress ratio of $R = 0.1$, and another scenario at $\sigma_{\max} = 110\text{MPa}$ and $R = 0.5$. More detailed information on the model and loading conditions can be found in the accompanying article (Lazzeri, Lanciotti, and Polese, 2009) that presents the experimental procedures in detail. The use of two different base materials (AA2024 and AA6056) in combination with four different manufacturing scenarios and two different loading conditions results in a large variety of different configurations, which were investigated experimentally as well as numerically using all techniques described in the previous sections to predict the fatigue crack growth behaviour.

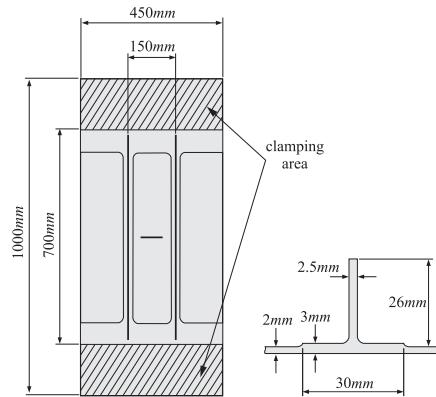


Figure 15: Geometry of investigated panel structure (DaToN panel)

The respective boundary conditions for each specific numerical technique is given in the associated subsections in section 2.

4.2 Stress intensity factor solutions

In the following sections the stress intensity factor solutions from the above presented simulation models will be presented for the 2-stiffener model geometry described in section 4.1. Making use of the symmetry of the model all following plots will only give the stress intensity factor for one crack tip, i.e. one half of the crack a . For the HSC panels, which showed no residual stresses, SIF results from all previously introduced simulation models are available. Since no residual stresses were considered for the p-FEM approach by IAI no results can be given for this approach for the welded panel configurations.

The basic stress intensity factor solution (without consideration of residual stresses) corresponds to the stress intensity factor caused by the global loading σ_0 while the SIF solutions for the welded configurations show the overall or effective stress intensity factor $K_{eff} = K_0 + K_{res}$ which also includes the stress intensity factor contribution K_{res} resulting from the residual stress field.

4.2.1 Basic SIF (without residual stresses)

The first result set to be presented represents the stress intensity factor solution without consideration of residual stresses which were determined using the basic approaches described in section 2 and is hence referred to as basic SIF solution. The resulting plots in Fig. 16 show the evolution of the mode I stress intensity fac-

tor with increasing (half) crack length a . For small and intermediate crack lengths

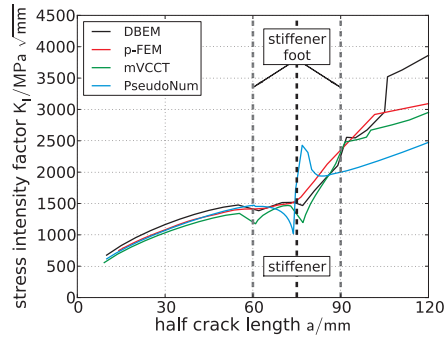


Figure 16: Stress intensity factor solutions at maximum load $\sigma_0 = 110\text{MPa}$ without RS (HSC)

up to approximately 55mm the stress intensity factors for all models lie within a relatively small range and show good accordance with the dual boundary element method (DBEM) showing slightly larger SIFs than the other models. Further approaching the stiffener position the results show increasing deviations. This can be attributed to the different capabilities of the models to represent the increased thickness at the stiffener foot which extends 15mm to both sides of the stiffener and corresponds to a half crack length of $a = 60\text{mm}$, which represents the position from which on larger deviations can be observed between the results. While the dual boundary element method and the 3D FE approach which uses the modified virtual crack closure technique show a significant decrease of the stress intensity factors, this decrease is not that significant for the two dimensional pFEM and analytical approach. The deviations between the numerical approaches then decrease again showing slightly increasing SIFs when the crack further approaches the stiffener but increase again once the crack reached the stiffener position ($a = 75\text{mm}$). The analytical approach (PseudoNum) shows a different characteristic within this region with constantly decreasing SIF values up to the stiffener position. Once the crack grows beyond the stiffener all simulations show steadily increasing SIF values up to failure with good accordance between the numerical approaches with larger discrepancies of the analytical approach which is attributed to the missing capabilities to account for transversal bending which is very pronounced for large skin crack lengths $a > 90\text{mm}$. However these effects do not have such an importance with respect to following fatigue crack growth simulations since the major portion of the whole fatigue life of the cracked 2 stiffener specimens is achieved

before the crack reaches the stiffener position. Therefore the focus for following SIF result discussions will be on the SIF solution results for crack lengths up to the stiffener position at $a = 75\text{mm}$.

4.2.2 Effective SIF considering residual stresses

As presented before several different approaches were investigated to incorporate the effects of residual stresses into the simulation models, which all have in common that they are aiming at a superposition of the stress intensity factors from global loading and residual stresses. All these approaches require experimentally or numerically determined residual stress field information in order to determine the residual stress intensity factor K_{res} , so that it is obvious that also the results are significantly depending on the residual stress field that is incorporated. Comparing the residual stress fields given in Figs. 14, 12 and 13 relatively large differences between the approximations can be observed for the region between the stiffeners which naturally will have an effect on the resulting stress intensity factors as will be discussed below. All approximations, like the experimental measurements, predict compressive residual stresses within this region but the absolute values and curve characteristics of the approximations differ significantly. These compressive residual stresses have a beneficial effect on the fatigue crack growth behaviour since they reduce the loading on the crack tip and hence reduce the effective stress intensity factor being determined by superposition of K_{res} and K_0 . This effect can be observed in Fig. 17 and Fig. 18 for the two different materials and the different welding conditions. Like before the result discussion will be focused on the SIF

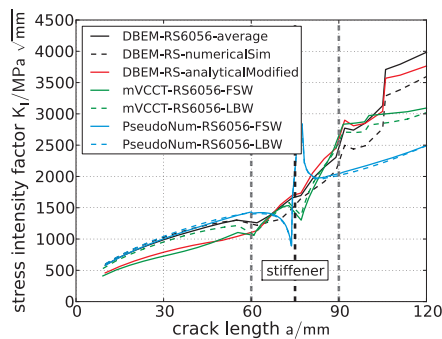


Figure 17: Stress intensity factor solutions at maximum load $\sigma_0 = 110\text{MPa}$ considering RS AA6056

results up to the stiffener position because of its major importance for subsequent

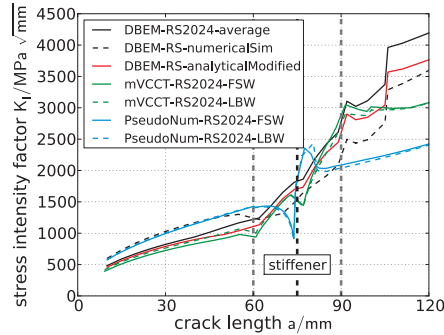


Figure 18: Stress intensity factor solutions at maximum load $\sigma_0 = 110\text{MPa}$ considering RS AA2024

fatigue crack growth calculations (see comments above). For both configurations two major regions can be identified where most of the stress intensity factor curves are located. For the AA6056 material configurations in Fig. 17 most configurations show a moderate decrease of the stress intensity factors approaching the stiffener and only two simulations show larger reductions. One of these simulations uses a transformed empirical formulation with maximum compressive residual stresses in the inter-stiffener region (region between the stiffeners) and can be regarded as an extreme case that probably overestimates the effect of residual stresses (cp. Fig. 14). The stress intensity factor results for the residual stress configurations of the AA2024 panels in Fig. 18 show the same general characteristics. However, it can be observed that there are two additional simulation combinations that now predict the more significant reduction of the effective stress intensity factors in comparison to the AA6056 simulations. The remaining simulations still show a rather moderate reduction of the SIF like could be observed for the majority of the simulations for AA6056.

An interesting fact to notice in Figs. 17 and 18 is that the simulations which use the basic empirical expressions proposed by Terada (1976) and Tada and Paris (1983) (cp. DBEM-Terada and the simulations using the pseudo numeric approach) give similar SIF solutions. In contrast to that the above mentioned modifications on the empirical formulation by Tada which are used for the analytical approaches (PseudoNum simulations) result in a better representation of the compressive residual stress field between the stiffeners (cp. Figs. 12 and 13) leading to reduced SIF for small crack lengths. These simulations also show good accordance with the results from the dual boundary element method (DBEM) in combination with the

numerically determined residual stress field.

5 Summary

This paper presented the applied simulation models that were used for stress intensity factor calculations during the numerical modelling work package of the EC funded project DaToN which was devoted to the experimental investigation and numerical modelling of metallic stiffened aircraft structures being manufactured by innovative manufacturing techniques like high speed cutting (HSC), laser beam welding (LBW) and friction stir welding (FSW). Herein, the incorporation of residual stress effects arising from the latter two joining techniques (LBW & FSW) was of special interest since these additional stress loading was found to have a considerable influence on the fatigue crack growth behaviour. Therefore, this first part focused in detail on the residual stress modelling approaches and their incorporation into the basic simulation models. For the two-stiffener panel configuration investigated within this study the stress intensity factor (SIF) simulation results, attained using these new modelling approaches, showed that residual stresses do have an effect on the stress intensity factors. It could be observed that the magnitude of this effect mainly depends on the residual stress input which is used for simulation while the effect of the different basic simulation approaches has only a minor effect. Part II uses the SIF results from this study to investigate the effects of the residual stresses on the fatigue crack growth behaviour, which is also compared in detail with fatigue crack growth results from experiments performed during the project. This also includes a presentation of crack growth models that can be used to incorporate the effects of residual stresses including the determination of the crack growth parameters to be used with these formulations.

Acknowledgement: The numerical techniques and results presented within this article were partly developed and acquired during the project "DaToN" which was funded by the European Commission within the 6th framework program. The required materials were generously provided by ALCAN. Both, the ECs financial support as well as ALCANS material support, is greatly acknowledged by all involved partners.

References

ABAQUS (2007): *ABAQUS user manual*.

Aliabadi, M. (2002): *The Boundary Element Method, vol II: application to solids and structures*. Chichester, Wiley.

- Diamantakos, A.; Tsirkas, S.** (2008): Thermo-mechanical residual stress simulations for daton panels. Technical report, University of Patras, 2008.
- Häusler, S. M.; Horst, P.** (2008): Fast analytical algorithm for fatigue crack life estimations of integrally stiffened metallic panels. *Key Engineering Materials*, vol. 385-387, pp. 529–532.
- Krueger, R.** (2002): The virtual crack closure technique: History, approach, and applications. Technical report, NASA/CR-2002-211628 ICASE Report No. 2002-10, 2002.
- Lanciotti, A.; Lazzeri, L.; Polese, C.** (2008): Residual stress measurement in daton panels. Technical report, University of Pisa, 2008.
- Lazzeri, L.; Lanciotti, A.; Polese, C.** (2009): Experimental survey of residual stress effects on fatigue crack growth in integrally stiffened aircraft structures. *Structural Durability and Health Monitoring*, vol. 100, pp. 100–110.
- Nishimura, T.** (1991): Stress intensity factors for a cracked stiffened sheet with cracked stiffeners. *Journal of Engineering Materials and Technology*, vol. 113, pp. 119–124.
- Rybicki, E.; Kanninen, M.** (1977): A finite element calculation of stress intensity factors by a modified crack closure integral. *Engineering Fracture Mechanics*, vol. 9, no. 4, pp. 931–938.
- Swift, T.** (1979): Damage tolerance analysis of redundant structures. In *Fracture Mechanics Design Methodology, AGARD-LS-97*.
- Tada, H.; Paris, P.** (1983): The stress intensity factor for a crack perpendicular to the welding bead. *International Journal of Fracture*, vol. 21, pp. 279–284.
- Tada, H.; Paris, P. C.; Irving, G. R.** (2000): *The stress analysis of cracks handbook*. ASME press, New York, 3 edition.
- Tavares, S.M.O. et al.** (2011): Crack growth simulation in integrally stiffened structures including residual stress effects from manufacturing. Part II: results and comparison with experiments. *Structural Durability and Health Monitoring*, vol. 100, pp. 135–150.
- Terada, H.** (1976): An analysis of stress intensity factor of a crack perpendicular to the welding bead. *Engineering Fracture Mechanics*, vol. 8, pp. 441–444.
- Terada, H.; Nakajima, T.** (1985): Analysis of stress intensity factor of a crack approaching welding bead. *International Journal of Fracture*, vol. 27, pp. 83–90.
- Wen, P.; Aliabadi, M.; Young, A.** (2004): Crack growth analysis for multi-layered airframe structures by boundary element method. *Engineering Fracture Mechanics*, vol. 71, pp. 619–631.

Wohlfahrt, H. (1987): Residual stresses as a consequence of welding. In *International Guidebook on Residual Stresses, Advances in Surface Treatments: Technology - Applications - Effects*, pp. 39–58. Pergamon Press, Oxford.

Appendix A: Comparison of experimental and empirical residual stress fields

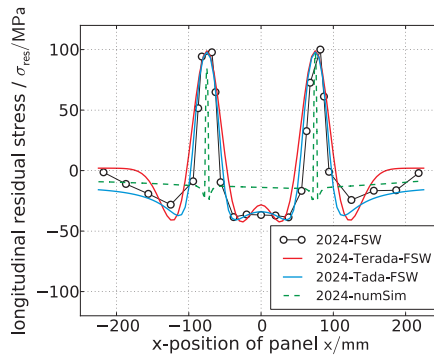


Figure 19: Experimental and empirical residual stress fields for AA2024-FSW used for the weight function method (PseudoNum)

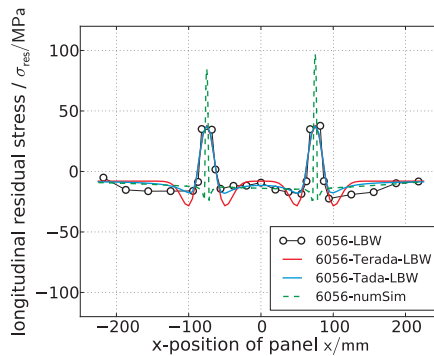


Figure 20: Experimental and empirical residual stress fields for AA6056-LBW used for the weight function method (PseudoNum)